

Magnetic Excitations in Spin-Orbit Coupled d^4 Mott Insulator on Square Lattice

Alireza Akbari and Giniyat Khaliullin

Max-Planck-Institut für Festkörperforschung, Heisenbergstrasse 1, D-70569 Stuttgart, Germany

(Dated: October 1, 2018)

We study the magnetic order and excitations in strong spin-orbit coupled, Van Vleck-type, d^4 Mott insulators on a square lattice. Extending the previous work, we include the tetragonal crystal field splitting and explore its effects on magnetic phase diagram and magnon spectra. Two different ordered phases, with in-plane and out-of-plane orientation of the staggered moments, are found for the higher and lower values of the crystal field splitting, respectively. The magnetic excitation spectra for paramagnetic and magnetically ordered phases are calculated and discussed in the context of a candidate spin-orbit d^4 Mott insulator Ca_2RuO_4 .

I. INTRODUCTION

In a solid, five-fold orbital degeneracy of a d -electron level is lifted by crystal field potential as well as by covalency effects. In case of local cubic symmetry, two subsets of d -orbitals with two-fold e_g and three-fold t_{2g} symmetry, separated by a large energy of the order of $10Dq \sim 2 - 3$ eV, are formed. The remaining degeneracy of orbitals – which adds up to that of spin – has to be lifted one way or another, involving dynamical Jahn-Teller effect and interionic exchange interactions. If the latter mechanism dominates, the spin and orbital degrees of freedom strongly couple to each other and are described by a family of so-called Kugel-Khomskii-type models¹.

General behavior of Kugel-Khomskii Hamiltonians is very complex because of the frustrated nature of orbital interactions, in particular in the case of t_{2g} orbitals where the higher degeneracy enhances quantum effects^{2,3}. In addition to that, t_{2g} triplet has an unquenched orbital angular momentum L , and relativistic spin-orbit coupling (SOC) $\lambda(\mathbf{S} \cdot \mathbf{L})$ is active. When λ is comparable to the strength of exchange interactions, spin-orbit coupling effects become of a nonperturbative nature. In that case, it is more convenient to represent the spin-orbital exchange Hamiltonians in terms of ionic multiplets in which SOC is already included⁴. Often, it is sufficient to keep the lowest-lying ionic multiplet with $2\tilde{S} + 1$ degeneracy; this results in effective, "pseudospin \tilde{S} " Hamiltonians describing low-energy magnetic properties of a material.

By construction, pseudospins \tilde{S} inherit the spatial shape and bond-directional nature of orbitals and their interactions³. Thus, the pseudospin Hamiltonians may strongly deviate from a conventional, spin-isotropic Heisenberg models, even in a simplest case of just twofold Kramers degeneracy with $\tilde{S} = 1/2$. As an example, exchange interactions between t_{2g}^5 ions with pseudospins $\tilde{S} = 1/2$ obtain large Ising term with an unusual, bond-dependent alternation of the "Ising-axes"^{3,5,6}, leading to unconventional magnetic states. The pseudospin Hamiltonians for $\tilde{S} > 1/2$ receive in addition strong biquadratic and multipolar interactions^{7,8}. Experimental studies of the iridium oxides hosting pseudospin physics⁹⁻¹¹ have boosted general interest in strong spin-orbit coupled

magnetism (see Ref. 12 for the recent review).

It may happen that the lowest spin-orbit ionic state has no degeneracy, $\tilde{S} = 0$, and hence it is nonmagnetic. Such is the case of transition metal ions with t_{2g}^4 configuration, where the spin $S = 1$ and orbital $L = 1$ moments form a singlet ground state¹³. Compounds with such nominally nonmagnetic ("Van Vleck-type") ions may still undergo magnetic transitions, due to mixing of the ground state $\tilde{S} = 0$ level with higher-lying $\tilde{S} = 1, 2$ multiplets by virtue of intersite exchange interactions¹⁴. Because of SOC, the transitions between multiplets with different \tilde{S} are magnetically active. In a solid, they become dispersive bands and have been observed in cobalt^{15,16} and iridium¹¹ oxides. Magnetic order in systems with $\tilde{S} = 0$ can be thus viewed as a Bose condensation of excitonic $\tilde{S} = 1$ band. A hallmark of such magnetism is the presence of soft amplitude mode¹⁷, corresponding here to the length fluctuations of the total angular momentum $\tilde{\mathbf{S}} = \mathbf{S} + \mathbf{L}$, in addition to conventional spin waves.

Theory of the exchange interactions and excitonic magnetism in Van Vleck-type t_{2g}^4 systems has been developed recently in Ref. 14, and ruthenium oxide Ca_2RuO_4 was suggested as a possible candidate material, based on the experimental observation¹⁸ of an unquenched SOC in this compound. In this paper, we consider magnetic order and excitations in more detail, with a particular focus on the effects of tetragonal distortion generally present in most perovskites.

II. MODEL HAMILTONIAN

Having in mind a layered perovskite structure of Ca_2RuO_4 , we consider square lattice of t_{2g}^4 ions which are assumed to have a low-spin configuration with spin $S = 1$ and orbital $L = 1$ moments. Intraionic SOC generates three levels at energies $0, \lambda, \text{ and } 3\lambda$, corresponding to the spin-orbit multiplets with total angular momentum $\tilde{S} = 0, 1, \text{ and } 2$. We neglect the highest, $\tilde{S} = 2$ multiplet at energy 3λ ; this is justified if the exchange interactions are not too strong as compared to SOC parameter λ . The remaining ionic degrees of freedom include ground state singlet $|s\rangle$ and $\tilde{S} = 1$ triplet $|T_{0,\pm 1}\rangle$ states. In a $|M_S, M_L\rangle$ basis, the wave-functions read as

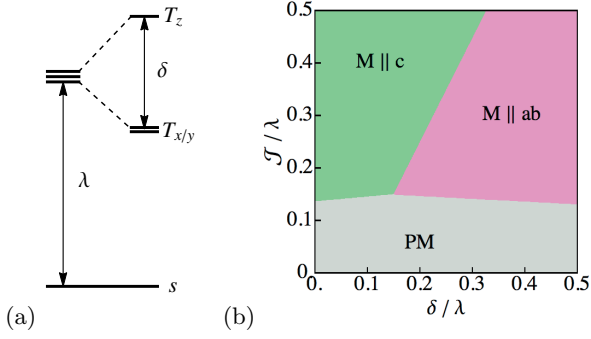


FIG. 1. (Color online) (a) Schematic of spin-orbit level structure including ground state singlet and a higher-lying pseudospin $\tilde{S} = 1$ triplet; the latter is split by tetragonal crystal field δ which favors in-plane orientation of magnetic moments. (b) Magnetic phase diagram as a function of exchange coupling and crystal-field splitting. It includes paramagnetic (PM) and two magnetic states with easy-axis ($M \parallel c$) and easy-plane ($M \parallel ab$) orderings.

$|s\rangle = \frac{1}{\sqrt{3}}(|1, -1\rangle - |0, 0\rangle + |-1, 1\rangle)$, $|T_0\rangle = \frac{1}{\sqrt{2}}(|1, -1\rangle - |-1, 1\rangle)$, $|T_{\pm 1}\rangle = \pm \frac{1}{\sqrt{2}}(|\pm 1, 0\rangle - |0, \pm 1\rangle)$. In calculations, the Cartesian components $T_x = \frac{1}{i\sqrt{2}}(T_1 - T_{-1})$, $T_y = \frac{1}{\sqrt{2}}(T_1 + T_{-1})$, and $T_z = iT_0$ are often more convenient. Tetragonal crystal field splits the triplet level as shown Fig. 1(a). We note that a positive $\delta > 0$ corresponds to compression of the octahedra along c axis (in a view of point-charge model), and its value is equal to the half of the tetragonal splitting between xy and xz/yz orbital levels, $\delta = (E_{xz/yz} - E_{xy})/2$, which would be expected in the limit of $\lambda = 0$.

The effective singlet-triplet model \mathcal{H}_{eff} that we consider below reads then as follows:

$$\mathcal{H}_{eff} = \mathcal{H}_{CF} + \lambda \sum_i n_i + \mathcal{J} \sum_{\langle ij \rangle_a} h_{ij}^{(a)} + \mathcal{J} \sum_{\langle ij \rangle_b} h_{ij}^{(b)}, \quad (1)$$

comprising a tetragonal crystal field contribution

$$\mathcal{H}_{CF} = \delta \sum_i \left(n_{iz} - \frac{1}{3} n_i \right), \quad (2)$$

a spin-orbit coupling energy λ of triplet states [second term in Eq. (1)], and, finally, the superexchange interactions [last two terms in Eq. (1)]. For the a -type bonds of square lattice, the interactions can be represented via the hard-core T -bosons as follows¹⁹:

$$h_{ij}^{(a)} = \mathbf{T}_i^\dagger \cdot \mathbf{T}_j - \frac{1}{3} T_{i,x}^\dagger T_{j,x} - \frac{5}{6} \mathbf{T}_i \cdot \mathbf{T}_j + \frac{1}{6} T_{i,x} T_{j,x} + h.c. \quad (3)$$

Interactions $h_{ij}^{(b)}$ on b -bonds are obtained by a substitution $T_{i,x} \rightarrow T_{i,y}$. In the above equations, $n = n_x + n_y + n_z$ with $n_\alpha = T_\alpha^\dagger T_\alpha$, and $\mathcal{J} = \frac{t_0^2}{U}$ represents the exchange energy scale. Note that $h^{(a,b)}$ represent the quadratic terms in T -boson interactions; full exchange Hamiltonian contains also three- and four-boson terms²⁰ which are neglected here. This approximation is valid near the critical points when density of condensed bosons is small. We

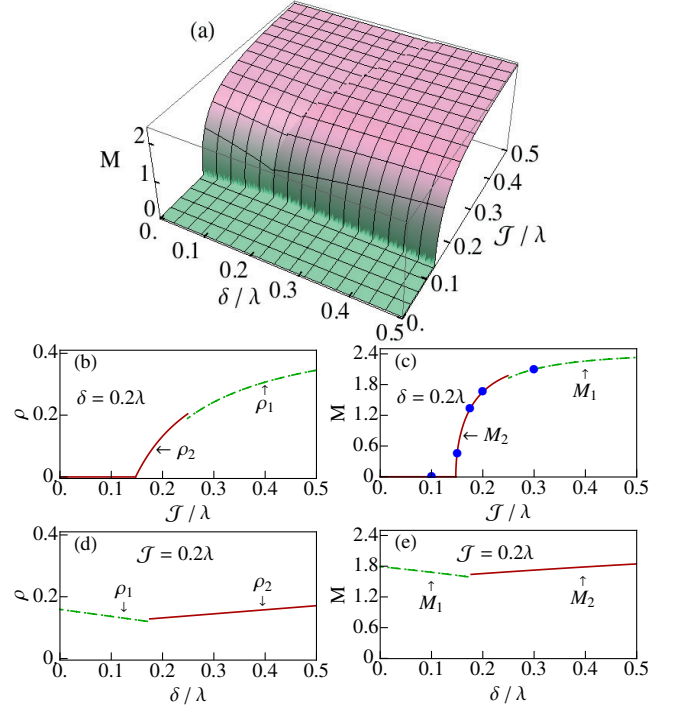


FIG. 2. (Color online) (a) The staggered magnetic moment M as a function of δ and \mathcal{J} . (b) The condensate density ρ and (c) the staggered moment M values versus exchange coupling \mathcal{J} , for the fixed crystal-field splitting $\delta = 0.2\lambda$. [The blue dots in panel (c) will be referred to later in Fig. 6]. (d) The condensate density ρ and (e) the staggered moment M values versus δ , for the fixed $\mathcal{J} = 0.2\lambda$.

note finally that T operators physically correspond to the singlet-triplet transitions between $\tilde{S} = 0$ and $\tilde{S} = 1$ levels. In other words, they are composite objects subject to the hard-core constraint $n_T \leq 1$, and can alternatively be represented as $\mathbf{T} \rightarrow s^\dagger \mathbf{t}$, via singlet s and triplet \mathbf{t} particles that obey the constraint $n_s + n_t = 1$.

III. GROUND STATE PROPERTIES

Depending on the relative strength of the exchange \mathcal{J} and SOC λ parameters, the ground state of effective Hamiltonian Eq. (1) can be either paramagnetic or antiferromagnetic. There are two different magnetic phases, with out-of-plane $M \parallel c$ and in-plane $M \parallel ab$ orientations of the staggered moments. The M -orientation is decided by the competition between the exchange \mathcal{J} and the crystal-field δ couplings. We calculate below classical energies of magnetically ordered states, and obtain from them a phase diagram and ordered moment values.

A. Phase diagram

Magnetic phase I ($M \parallel c$): This state is obtained by a condensation of the T_z -component of $\tilde{S} = 1$ triplet: $T_z \rightarrow \sqrt{\rho_1}$. The corresponding classical energy gain is:

$$E_{g1} = -\rho_1\mu_1 = -\frac{1}{4\kappa_1}(\kappa_1 - \beta_1)^2, \quad (4)$$

where $\rho_1 = \frac{1}{2}(1 - \frac{\beta_1}{\kappa_1})$ is the condensate density, and $\mu_1 = \frac{1}{2}(\kappa_1 - \beta_1)$. We note that the constant $-\mu$ has a physical meaning of chemical potential. The condensate density and hence the magnetic moments are determined by the interaction parameters $\kappa_1 = \frac{22}{3}\mathcal{J}$ and $\beta_1 = \lambda + \frac{2}{3}\delta$. The magnetic phase transition sets in at $\kappa_1 = \beta_1$ (i.e., when μ_1 becomes zero); this gives the critical value of the exchange constant \mathcal{J} as $\mathcal{J}_1^c = (3\lambda + 2\delta)/22$.

Magnetic phase II ($M \parallel ab$): The magnetic moment is in the ab -plane corresponding to the condensation of $T_x \rightarrow \sqrt{\rho_2}$. The ground state energy can be represented in the form as above,

$$E_{g2} = -\rho_2\mu_2 = -\frac{1}{4\kappa_2}(\kappa_2 - \beta_2)^2, \quad (5)$$

but with different parameters: $\rho_2 = \frac{1}{2}(1 - \frac{\beta_2}{\kappa_2})$ and $\mu_2 = \frac{1}{2}(\kappa_2 - \beta_2)$, where $\kappa_2 = \frac{19}{3}\mathcal{J}$ and $\beta_2 = \lambda - \frac{1}{3}\delta$. The magnetic phase transition line is given by $\kappa_2 = \beta_2$, and the critical value $\mathcal{J}_2^c = (3\lambda - \delta)/19$.

Using the above results, we find a phase diagram as shown in Fig. 1(b). At small crystal fields δ , the exchange anisotropy terms in Eq. (3) select out-of-plane M -direction. However, already quite small tetragonal splitting δ stabilizes the in-plane magnetic order, which corresponds to the case of Ca_2RuO_4 .

B. Staggered Magnetisation

The magnetic moment of present singlet-triplet system is represented by the following operator¹⁴:

$$\mathbf{M} = -i\sqrt{6}(\mathbf{T} - \mathbf{T}^\dagger) - ig_J(\mathbf{T}^\dagger \times \mathbf{T}), \quad (6)$$

with $g_J = 1/2$. In magnetic phases with condensed bosons, the first term of this operator obtains finite expectation value [at the ordering wave-vector (π, π)]. Using the above results for condensate amplitudes, we find that the staggered magnetic moment in phase I is:

$$M_1 = \sqrt{6(1 - \eta_1)}; \quad \mathcal{J} > \mathcal{J}_1^c, \quad (7)$$

where $\eta_1 = \beta_1^2/\kappa_1^2$. The same equation holds for the magnetic moment in phase II, but with $\eta_2 = \beta_2^2/\kappa_2^2$ and $\mathcal{J} > \mathcal{J}_2^c$. Parameters $\beta_{1,2}$ and $\kappa_{1,2}$ have been given above.

The numerical results for the staggered moment as a function of parameters δ and \mathcal{J} are shown in Fig. 2. A

clear trace of the phase transition from PM to magnetic phases, and a discontinuous spin-reorientation transition between phases I and II are observed.

Condensate densities [Fig. 2(b)] and staggered moments [Fig. 2(c)] critically depend on \mathcal{J}/λ ratio. However, they are not sensitive to the value of anisotropy parameter δ [Fig. 2(d,e)] whose major effect is the stabilization of phase II with in-plane magnetic moments.

IV. EXCITATION SPECTRA

A. Magnon dispersions

We consider now spin excitations above the ground state. Technically, we follow early works^{21,22} which extended a linear spin-wave theory to singlet-triplet models. We handle the particle-number constraint on average only, neglecting magnon interaction effects.

Within this approximation, spin excitations in the paramagnetic phase follow directly from Eqs. (1-3), after the Bogoliubov transformation of the T operators (in momentum space). For T_z component, this gives

$$\omega_z(\mathbf{k}) = (\lambda + \frac{2}{3}\delta)\sqrt{1 + a_z\phi_{\mathbf{k}}}, \quad a_z = \frac{22\mathcal{J}}{3\lambda + 2\delta}, \quad (8)$$

where $\phi_{\mathbf{k}} = \frac{1}{2}(\cos k_x + \cos k_y)$ is a square lattice form-factor. Because of tetragonal symmetry, the T_x and T_y modes are degenerate:

$$\omega_{x/y}(\mathbf{k}) = (\lambda - \frac{1}{3}\delta)\sqrt{1 + a_{x/y}\phi_{\mathbf{k}}}, \quad a_{x/y} = \frac{19\mathcal{J}}{3\lambda - \delta}. \quad (9)$$

For the antiferromagnetically ordered phases, we introduce two sublattices labeled by A and B. It is convenient also to introduce the sublattice dependent phase shifts $T_A \rightarrow iT$, $T_B \rightarrow -iT$, and work within the extended Brillouin zone (BZ). Then, after the Fourier transformation $\mathbf{T}_{\mathbf{k}} = \sum_i e^{-i\mathbf{k}\cdot\mathbf{r}_i}\mathbf{T}_i$ in Eqs. (1-3), we arrive at the following momentum-space Hamiltonian:

$$\begin{aligned} \mathcal{H} &= \sum_{\mathbf{k}} (\mathcal{H}_{\mathbf{k}}^z + \mathcal{H}_{\mathbf{k}}^x + \mathcal{H}_{\mathbf{k}}^y) \\ &= \sum_{\mathbf{k}} \left(\lambda + \frac{2}{3}\delta - 4\mathcal{J}\phi_{\mathbf{k}} \right) T_{\mathbf{k},z}^\dagger T_{\mathbf{k},z} - \frac{5}{3}\mathcal{J}\phi_{\mathbf{k}} (T_{\mathbf{k},z} T_{\mathbf{k},z} + h.c.) \\ &\quad + \left[\left(\lambda - \frac{1}{3}\delta + \frac{10}{3}\mathcal{J}\phi_{\mathbf{k}} \right) T_{\mathbf{k},x}^\dagger T_{\mathbf{k},x} - \frac{3}{2}\mathcal{J}\phi_{\mathbf{k}} (T_{\mathbf{k},x} T_{\mathbf{k},x} + h.c.) \right] \\ &\quad + [x \rightarrow y], \end{aligned} \quad (10)$$

Magnetic order in singlet-triplet models implies condensation of a particular component of the triplet state, i.e., it mixes-up coherently with the ground state singlet. In order to describe this process, we introduce $\mathbf{T} \rightarrow s^\dagger \mathbf{t}$ with $n_s + n_t = 1$, and transform the basis as follows:

$$\begin{aligned} t_\alpha &= \tilde{s} \sin \theta + \tilde{t}_\alpha \cos \theta, \\ s &= \tilde{s} \cos \theta - \tilde{t}_\alpha \sin \theta, \end{aligned} \quad (11)$$

where $\alpha = z(x)$ for phase I (II). A new \tilde{s} boson is then condensed. Fluctuations of t_α represent amplitude fluctuations, while remaining two (uncondensed) components of the triplet become transverse magnons. The basis-rotation angle θ is determined by minimization of the classical energy E_g of Hamiltonian Eq. (10), which results in $\sin\theta = \sqrt{\rho}$ and $E_g = -\rho\mu$, with condensate densities $\rho_{1,2}$ and potentials $-\mu_{1,2}$ for phases I and II, correspondingly, as given in a previous section.

We consider first the magnetic phase I. After the above transformations, quadratic part of the Hamiltonian Eq. (10) takes the following form:

$$\mathcal{H}_k^z = \mathcal{A}_k^z \tilde{t}_{\mathbf{k},z}^\dagger \tilde{t}_{\mathbf{k},z} + \frac{1}{2} \mathcal{B}_k^z (\tilde{t}_{\mathbf{k},z} \tilde{t}_{-\mathbf{k},z} + h.c.), \quad (12)$$

where

$$\begin{aligned} \mathcal{A}_k^z &= \kappa_1 \left[1 + \frac{\phi_{\mathbf{k}}}{22} (1 + 11\eta_1) \right], \\ \mathcal{B}_k^z &= \kappa_1 \left[\frac{\phi_{\mathbf{k}}}{22} (1 - 11\eta_1) \right]. \end{aligned} \quad (13)$$

Diagonalization of Eq. (12) gives the amplitude mode dispersion:

$$\omega_z(\mathbf{k}) = \sqrt{(\mathcal{A}_k^z - \mathcal{B}_k^z)(\mathcal{A}_k^z + \mathcal{B}_k^z)} = \sqrt{\kappa_1^2 + \beta_1^2 \phi_{\mathbf{k}}}. \quad (14)$$

The transverse components $t_{x/y}$ are degenerate in phase I. Accounting for the chemical energy shift $-\mu(n_x + n_y)$, we find the corresponding quadratic Hamiltonian for x/y modes in a form of Eq. (12) again, with the following constants

$$\begin{aligned} \mathcal{A}_k^x &= \mathcal{A}_k^y = \bar{\kappa}_1 - \delta + \frac{5}{11} \bar{\kappa}_1 \phi_{\mathbf{k}}, \\ \mathcal{B}_k^x &= \mathcal{B}_k^y = \frac{9}{22} \bar{\kappa}_1 \phi_{\mathbf{k}}, \end{aligned} \quad (15)$$

where $\bar{\kappa}_1 = (\kappa_1 + \beta_1)/2$. This gives spin-wave dispersions

$$\omega_{x/y}(\mathbf{k}) = (\bar{\kappa}_1 - \delta) \sqrt{1 + \frac{19}{22} \frac{\bar{\kappa}_1 \phi_{\mathbf{k}}}{(\bar{\kappa}_1 - \delta)}} \quad (16)$$

for the magnetic phase I with $M \parallel c$.

For the magnetic phase II, similar calculations give the following results for the energy-momentum dispersions of the amplitude (x) and transverse (y, z) modes:

$$\begin{aligned} \omega_x(\mathbf{k}) &= \sqrt{\kappa_2^2 + \beta_2^2 \phi_{\mathbf{k}}}, \\ \omega_y(\mathbf{k}) &= \bar{\kappa}_2 \sqrt{1 + \phi_{\mathbf{k}}}, \\ \omega_z(\mathbf{k}) &= (\bar{\kappa}_2 + \delta) \sqrt{1 + \frac{22}{19} \frac{\bar{\kappa}_2 \phi_{\mathbf{k}}}{(\bar{\kappa}_2 + \delta)}}. \end{aligned} \quad (17)$$

It is noticed that in phase II with $M \parallel ab$, there is no degeneracy of magnon branches, i.e., in-plane (y) and out-of-plane (z) magnons are split.

Some examples of magnon dispersion curves, representing different magnetic phases, are plotted in Figs. 3

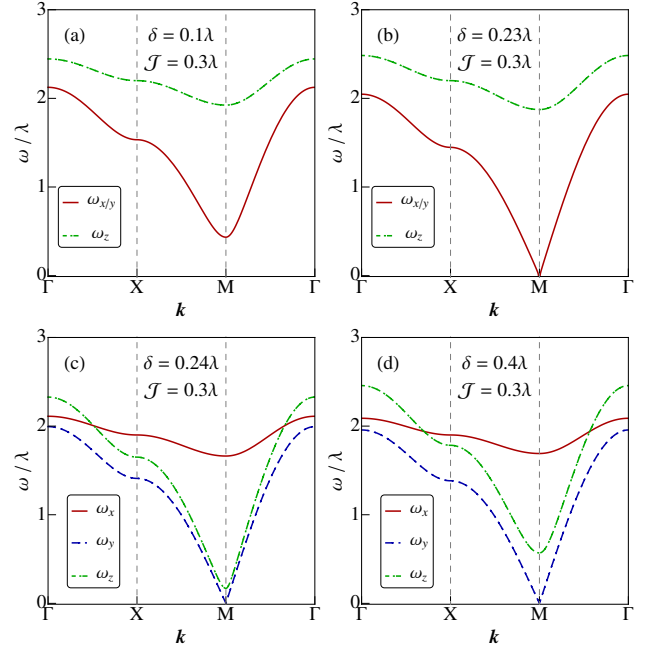


FIG. 3. (Color online) The excitation energies ω_α (in units of SOC constant λ) versus momentum \mathbf{k} , for fixed $\mathcal{J} = 0.3\lambda$ and different δ values: (a) $\delta = 0.1\lambda$, (b) $\delta = 0.23\lambda$, (c) $\delta = 0.24\lambda$, and (d) $\delta = 0.3\lambda$. Panels (a-b) represent the phase I, and (c-d) represent the phase II. Here, $\Gamma = (0, 0)$, $X = (0, \pi)$ and $M = (\pi, \pi)$.

and 4. Fig. 3 shows the evolution of excitation spectra as a function of the crystal-field parameter δ , and their dependence on the exchange parameter \mathcal{J} is illustrated in Fig. 4. The features mentioned above such as a separation of the amplitude mode from the low-energy magnon modes, and splitting of the latter into two distinct branches in phase II can be noticed.

In order to see the evolution of the magnon gaps in more detail, we plot in Fig. 5 the magnetic excitation energies at the Bragg point $\mathbf{Q} = (\pi, \pi)$, as a function of the exchange constant \mathcal{J} at different δ values. In the PM phase (small \mathcal{J}), all the branches have a finite gap. At the critical value of \mathcal{J} , gap for the amplitude mode closes. Further increase of \mathcal{J} enhances the excitation gaps for all the branches in phase I [see panel (a)]. In phase II, there remains gapless Goldstone mode [see panels (b-d)], corresponding to a free rotation of the staggered moment within ab plane. Figs. 5(b) and (c) illustrate a transformation of spin-wave dispersions at the first order phase transitions between phases I and II.

B. Magnon Intensities

The intensity of spin excitations is given by the imaginary part the dynamic spin susceptibility which, within the present linear spin-wave approximation, takes the fol-

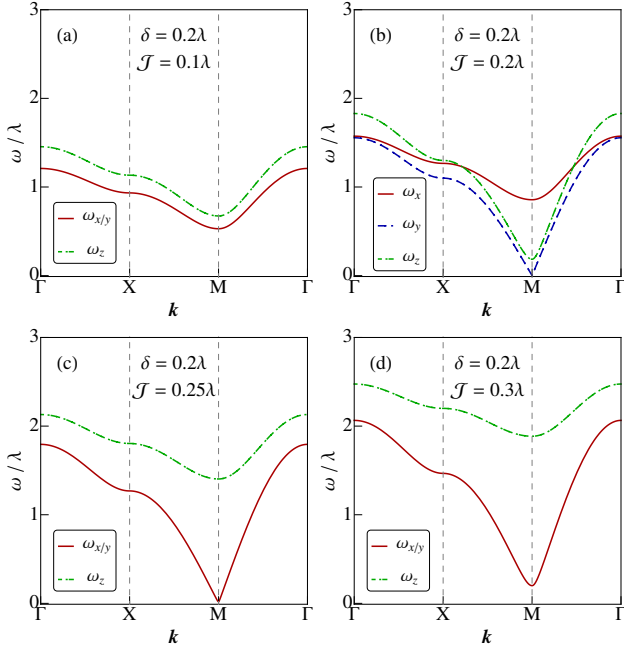


FIG. 4. (Color online) The same as the Fig. 3 but for fixed $\delta = 0.2\lambda$ and different \mathcal{J} values: (a) $\mathcal{J} = 0.1\lambda$, (b) $\mathcal{J} = 0.2\lambda$, (c) $\mathcal{J} = 0.25\lambda$, and (d) $\mathcal{J} = 0.3\lambda$. Panel (a) corresponds to the paramagnetic phase, (b) represents the phase II, and (c-d) represent the phase I.

lowing form:

$$\text{Im}\chi_{\mathbf{q}}^{\gamma}(\omega) = \frac{|F_{\gamma}(\mathbf{q})|}{\omega_{\gamma}(\mathbf{q})} \delta(\omega - \omega_{\gamma}(\mathbf{q})). \quad (18)$$

In the paramagnetic phase, the factors $F_{\gamma}(\mathbf{q})$ representing the spectral weights of $\gamma = x, y, z$ magnon modes are given by

$$F_x(\mathbf{q}) = F_y(\mathbf{q}) = \frac{54\bar{\kappa}_2}{19}\phi_{\mathbf{q}}; \quad F_z(\mathbf{q}) = \frac{30\bar{\kappa}_1}{11}\phi_{\mathbf{q}}. \quad (19)$$

In the magnetic phase I, we have

$$\begin{aligned} F_x(\mathbf{q}) = F_y(\mathbf{q}) &= \frac{27\bar{\kappa}_1}{11}\phi_{\mathbf{q}}; \\ F_z(\mathbf{q}) &= \frac{3\bar{\kappa}_1}{11}(-1 + 11\eta_1)\phi_{\mathbf{q}}, \end{aligned} \quad (20)$$

and, finally, for the magnetic phase II, we obtain

$$\begin{aligned} F_x(\mathbf{q}) &= \frac{3\bar{\kappa}_2}{19}(-1 + 19\eta_2)\phi_{\mathbf{q}}; \\ F_y(\mathbf{q}) &= \frac{54\bar{\kappa}_2}{19}\phi_{\mathbf{q}}; \\ F_z(\mathbf{q}) &= \frac{60\bar{\kappa}_2}{19}\phi_{\mathbf{q}}. \end{aligned} \quad (21)$$

Magnon intensities are given by $I(\mathbf{q}, \omega) = \sum_{\gamma} \text{Im}\chi_{\mathbf{q}}^{\gamma}(\omega)$. The contour plots of this quantity, multiplied by $\sqrt{\omega}$ for clarity, are shown in Fig. 6. In the $(\mathcal{J} - \delta)$ parameter space, five different panels in this figure correspond to the

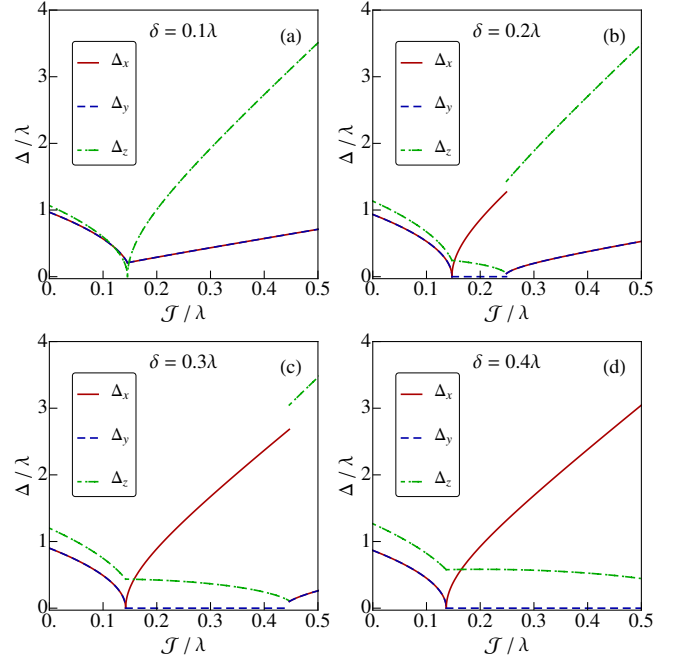


FIG. 5. (Color online) The excitation energy gaps at the Bragg (M) point, $\Delta = \omega(\mathbf{Q})$, as a function of exchange interaction \mathcal{J} , for different values of crystal-field parameter: (a) $\delta = 0.1\lambda$, (b) $\delta = 0.2\lambda$, (c) $\delta = 0.3\lambda$, (d) $\delta = 0.4\lambda$.

blue points in Fig. 2(c), and thus represent (a) the paramagnetic phase, (b-d) the magnetic phase II ($M \parallel ab$), and, finally, (e) the magnetic phase I ($M \parallel c$).

In PM phase, the intensities of all (degenerate x/y , and z) modes are nearly equal. In phase II [panels (b-d)], which is of particular interest in the context of Ca_2RuO_4 , the intensity of the highest energy (amplitude) mode is large near the critical point [see inset in panel (b)], but it fades away rather quickly at larger \mathcal{J} values.

V. APPLICATION TO Ca_2RuO_4

The calcium ruthenate, Ca_2RuO_4 , has a layered perovskite structure similar to that of La_2CuO_4 cuprate, and shows a Mott-insulating behavior below room temperature^{23,24}. It undergoes a magnetic phase transition at ~ 110 K, below which an antiferromagnetic order with a staggered moment $M \simeq 1.3 \mu_B$ is observed²⁵. A sizeable value of LS -product indicates that SOC is not quenched¹⁸, and hence this material may exhibit some features of the "excitonic" magnetism considered above. To our knowledge, no dynamical spin susceptibility measurements for Ca_2RuO_4 have been reported to date; some theoretical expectations are given below.

Observed ab -plane orientation of the moments²⁵ is consistent with the phase II in Fig. 1(b), which is stabilized by a compressive tetragonal distortion present in Ca_2RuO_4 .

One can roughly estimate the parameters \mathcal{J}/λ and

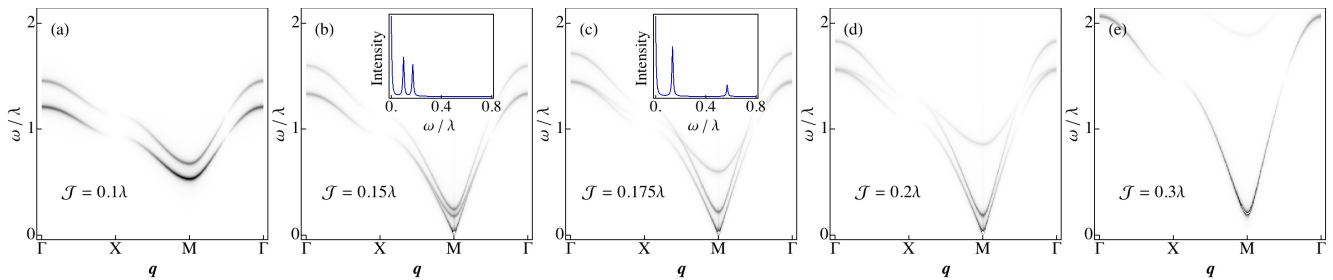


FIG. 6. (Color online) Contour maps of the magnon intensities (multiplied by $\sqrt{\omega}$ for better visibility), $\sqrt{\omega} I(\mathbf{q}, \omega) = \sqrt{\omega} \text{Im}\chi_{\mathbf{q}}(\omega)$, for constant $\delta = 0.2\lambda$ and different values of \mathcal{J} : (a) $\mathcal{J} = 0.1\lambda$, (b) $\mathcal{J} = 0.15\lambda$, (c) $\mathcal{J} = 0.175\lambda$, (d) $\mathcal{J} = 0.2\lambda$ and (e) $\mathcal{J} = 0.3\lambda$. Note that (a) belongs to paramagnetic phase, (b-d) represent the magnetic phase II, and (e) represents the magnetic phase I [see the blue points in Fig. 2(c)]. The insets in (b) and (c) show a direct comparison of the intensities $I(\mathbf{Q}, \omega)$ of three modes at the ordering wave-vector (M -point). The highest peak corresponds to the amplitude mode, the middle one represents out-of-plane magnon, and the lowest peak is in-plane magnon (which is gapless hence not properly shown for numerical reasons).

δ/λ from the observed staggered moment $M \simeq 1.3 \mu_B^{25}$ and the static magnetic susceptibility $\chi \simeq 2.6 \times 10^{-3} \text{emu/mol}^{25}$. The moment M is determined by η_2 [see Eq. (7)] defining the distance to the critical point, while the susceptibility is given by

$$\chi_{ab} = \frac{12\mu_B^2 N_A}{\kappa_2(1 + \eta_2)}, \quad (22)$$

where N_A is Avogadro number. From the M and χ equations, we find $\eta_2 \simeq 0.85$, and estimate the parameters $\mathcal{J}/\lambda \sim 0.17$, and $\delta/\lambda \sim 0.2$. Magnon dispersions in Ca_2RuO_4 are then expected to resemble the plots shown in Fig. 6(b,c). These plots suggest a full magnon bandwidth of the order of $1.5\lambda \sim 100 \text{ meV}$, given a spin-orbit coupling constant $\lambda(= \xi/2) \simeq 75 \text{ meV}^{18}$. The parameter $\mathcal{J} = \frac{t_0^2}{U} \simeq 13 \text{ meV}$ which follows from these estimates seems reasonable for t_{2g} systems with $t_0 \sim 0.2 \text{ eV}$ and $U \sim 3 \text{ eV}$. As far as the amplitude mode is concerned, the insets in Fig. 6 suggest a sizeable intensities; however, it might be difficult to identify this mode because it falls in the phonon-energy window ($\sim 40 \text{ meV}$).

VI. SUMMARY

We have studied here the phase diagram and magnetic excitations in Van Vleck-type d^4 Mott insulators with spin-orbit singlet ground state. As the intersite exchange interactions increase, the system makes a transition into an antiferromagnetically ordered state. For a square lattice geometry considered here, the exchange anisotropy supports a uniaxial-type magnetic order. Under a compressive strain, this order changes to the easy-plane one via a first order phase transition. We have calculated magnetic excitations over an entire phase diagram, quantifying the magnon dispersions and their intensities. We hope that the results presented here will motivate experimental studies of Ca_2RuO_4 and other potential candidate materials for excitonic-type magnetism²⁶ by means of inelastic neutron and/or resonant x-ray scattering techniques.

We would like to thank B.J. Kim for useful discussions.

¹ K.I. Kugel and D.I. Khomskii, Sov. Phys. Usp. **25**, 231 (1982).

² G. Khaliullin and S. Maekawa, Phys. Rev. Lett. **85**, 3950 (2000).

³ G. Khaliullin, Prog. Theor. Phys. Suppl. **160**, 155 (2005).

⁴ R.J. Elliott and M.F. Thorpe, J. Appl. Phys. **39**, 802 (1968).

⁵ G. Jackeli and G. Khaliullin, Phys. Rev. Lett. **102**, 017205 (2009).

⁶ J. Chaloupka, G. Jackeli, and G. Khaliullin, Phys. Rev. Lett. **105**, 027204 (2010); **110**, 097204 (2013).

⁷ G.-W. Chern and N. Perkins, Phys. Rev. B **80**, 180409(R) (2009).

⁸ G. Chen and L. Balents, Phys. Rev. B **84**, 094420 (2011).

⁹ B.J. Kim, H. Jin, S.J. Moon, J.-Y. Kim, B.-G. Park,

C.S. Leem, J. Yu, T.W. Noh, C. Kim, S.-J. Oh, J.-H. Park, V. Durairaj, G. Cao, and E. Rotenberg, Phys. Rev. Lett. **101**, 076402 (2008).

¹⁰ B.J. Kim, H. Ohsumi, T. Komesu, S. Sakai, T. Morita, H. Takagi, and T. Arima, Science, **323**, 1329 (2009).

¹¹ Jungho Kim, D. Casa, M.H. Upton, T. Gog, Y.-J. Kim, J.F. Mitchell, M. van Veenendaal, M. Daghofer, J. van den Brink, G. Khaliullin, and B.J. Kim. Phys. Rev. Lett. **108**, 177003 (2012).

¹² W. Witczak-Krempa, G. Chen, Y.B. Kim, and L. Balents, Annu. Rev. Condens. Matter Phys. **5**, 57 (2014).

¹³ A. Abragam and B. Bleaney, *Electron Paramagnetic Resonance of Transition Ions* (Clarendon, Oxford, 1970).

¹⁴ G. Khaliullin, Phys. Rev. Lett. **111**, 197201 (2013).

¹⁵ T.M. Holden, W.J.L. Buyers, E.C. Svensson, R.A. Cow-

- ley, M.T. Hutchings, D. Hukin, and R.W.H. Stevenson, *J. Phys. C: Solid St. Phys.* **4**, 2127 (1971).
- ¹⁶ W.J.L. Buyers, T.M. Holden, E.C. Svensson, R.A. Cowley, and M.T. Hutchings, *J. Phys. C: Solid St. Phys.* **4**, 2139 (1971).
- ¹⁷ T. Giamarchi, Ch. Rüegg, and O. Tchernyshyov, *Nat. Phys.* **4**, 198 (2008).
- ¹⁸ T. Mizokawa, L.H. Tjeng, G.A. Sawatzky, G. Ghiringhelli, O. Tjernberg, N.B. Brookes, H. Fukazawa, S. Nakatsuji, and Y. Maeno, *Phys. Rev. Lett.* **87**, 077202 (2001).
- ¹⁹ Alternatively, one can represent Eq. (3) also in terms of real fields \mathbf{u} and \mathbf{v} , defined as $\mathbf{T} = \mathbf{u} + i\mathbf{v}$ ¹⁴. In the $\mathbf{u} - \mathbf{v}$ representation, Eq. (3) coincides with the corresponding quadratic part of the exchange Hamiltonian (2) of Ref. 14. We also note that Ref. 14 has further replaced the bond-dependent terms by their average [see Eq. (3) of Ref. 14]; we do not use this approximation here.
- ²⁰ See second and third lines in Eq. (2) of Ref. 14.
- ²¹ T. Sommer, M. Vojta, and K.W. Becker, *Eur. Phys. J. B* **23**, 329 (2001).
- ²² M. Matsumoto, B. Normand, T.M. Rice, and M. Sigrist, *Phys. Rev. B* **69**, 054423 (2004).
- ²³ S. Nakatsuji, S. Ikeda, and Y. Maeno, *J. Phys. Soc. Jpn.* **66**, 1868 (1997).
- ²⁴ G. Cao, S. McCall, M. Shepard, J.E. Crow, and R.P. Guertin, *Phys. Rev. B* **56**, R2916 (1997).
- ²⁵ M. Braden, G. André, S. Nakatsuji, and Y. Maeno, *Phys. Rev. B* **58**, 847 (1998).
- ²⁶ G. Cao, T.F. Qi, L. Li, J. Terzic, S.J. Yuan, L.E. DeLong, G. Murthy, and R.K. Kaul, *Phys. Rev. Lett.* **112**, 056402 (2014).